Available online at www.sciencedirect.com
SCIENCE DIRECT®
International Journal of Heat and Mass Transfer 48 (2005) 2429–2442
International Journal of HEAT and MASS TRANSFER
www.elsevier.com/locate/ijhmt

Time and space resolved wall temperature and heat flux measurements during nucleate boiling with constant heat flux boundary conditions

Jerry G. Myers [a], Vamsee K. Yerramilli [b], Sam W. Hussey [a], Glenda F. Yee [a], Jungho Kim [b,*]

[a] National Aeronautics and Space Administration, Glenn Research Center at Lewis Field, 21000 Brookpark Road, Cleveland, OH 44135, USA
[b] Department of Mechanical Engineering, University of Maryland, College Park, MD 20742, USA

Received 1 September 2004; received in revised form 30 December 2004
Available online 19 March 2005

Abstract

The lack of time and space resolved measurements under nucleating bubbles has complicated efforts to fully explain pool-boiling phenomena. In this work, time and space resolved temperature and heat flux distributions under nucleating bubbles on a constant heat flux surface were obtained using a 10×10 microheater array with 100 μm resolution along with high-speed images. A numerical simulation was used to compute the substrate conduction, which was then subtracted from the heater power to obtain the wall-to-liquid heat transfer. The data indicated that most of the energy required for bubble growth came from the superheated layer around the bubble. Microlayer evaporation and contact line heat transfer accounted for not more than 23% of the total heat transferred from the surface. The dominant heat transfer mechanism was transient conduction into the liquid during bubble departure. Bubble coalescence was not observed to transfer a significant amount of heat.

Keywords: Boiling; Microheater array; Microconvection; Evaporation; Microlayer

1. Introduction

Investigations into single bubble pool boiling phenomena are often complicated by difficulties in obtaining time and space resolved information in the bubble region since the heaters and diagnostics used to measure heat transfer data are often on the order of, or larger than, the bubble characteristic length or region of influence. This has contributed to the development of many different and often contradictory models of pool boiling phenomena and conclusions about which mechanisms dominate.

Mikic and Rosenhow [1] proposed a transient conduction model in which the departing bubble removed a portion of the superheated liquid layer twice the bubble departure diameter. Cold, bulk liquid was assumed to rewet the surface immediately after bubble departure and transient conduction into this liquid occurred until nucleation of the next bubble. Cooper and Lloyd [2]

* Corresponding author. Tel.: +1 301 405 5437; fax: +1 301 314 9477.
E-mail address: kimjh@eng.umd.edu (J. Kim).

0017-9310/$ - see front matter © 2005 Elsevier Ltd. All rights reserved.
doi:10.1016/j.ijheatmasstransfer.2004.12.050

Nomenclature

A_h	heater area [m^2]
C_p	specific heat [J/kg °C]
d_{eq}	equivalent diameter [m]
h_{fg}	heat of vaporization [J/kg]
i	index
i_{heater}	heater current [A]
Ja	Jakob number, $=C_p\Delta T_{sat}/h_{fg}$
k	thermal conductivity [W/m °C]
P_{cr}	critical pressure [Pa]
P_r	reduced pressure
$\dot{q}$	power [W]
$\dot{q}''$	heat flux [W/m^2]
$\dot{q}''_h$	heater heat flux [W/m^2]
r,r'	radius [m]
r_0	initial radius [m]
t	time [s]
TCR	temperature coefficient of resistance [°C^{-1}]
T_{cr}	critical temperature [°C]
T_l	bulk liquid temperature [°C]
T_{liquid}	rewetting liquid temperature [°C]
T_r	reduced temperature
T_w	wall temperature [°C]
v	speed of contact line [m/s]
V_{top}	voltage at top of bridge [V]
V_{heater}	voltage across heater [V]
v_r	reduce volume
z	coordinate perpendicular to substrate surface [m]

Greek symbols

α_l	liquid thermal diffusivity [m^2/s]
ΔT_{sat}	wall superheat [°C]
γ	scaling factor
ρ_v	density of vapor [kg/m^3]

measured wall temperature variations under bubbles using micro-thermocouples, and proposed that bubble heat transfer occurred through the formation and evaporation of a thin liquid layer (the microlayer) between the growing bubble and the wall. Stephan and Hammer [3] proposed that heat transfer occurred primarily at the three-phase contact line where the liquid–vapor interface approaches the wall according to the mechanism proposed by Wayner et al. [4].

Yaddanapudi and Kim [5] measured local heat transfer underneath single bubbles nucleating periodically from a single site for saturated FC-72 at 1 atm (T_{sat} = 56.7 °C) with the wall held at a *constant wall temperature* of 79 °C using a microheater array with individual heaters 270 μm in size. The bubble departure diameter was about 370 μm, only slightly larger than a single heater. Their results indicated that bubble growth occurred primarily due to energy gained from the superheated liquid layer. Bubble departure resulted in rewetting of the wall by colder liquid, and heat transfer through transient conduction and/or microconvection. Although details of the model of Mikic and Rosenhow [1] were not supported by the data (e.g., the size of the superheated liquid layer removed by the departing bubble was only half the bubble departure diameter), the main assumption of transient conduction being the primary heat transfer mechanism was validated.

Demiray and Kim [6] presented local heat transfer data underneath bubbles nucleating from a single site under conditions similar to Yaddanapuddi and Kim [5], but their array consisted of 100 μm heaters which allowed good spatial resolution underneath the growing and departing bubbles. The surface temperature of the heater array and the bulk fluid temperature were held constant at 76 °C and 52 °C, respectively. Bubbles that nucleated at this site alternated between two modes: single bubble mode and multiple bubble mode. In single bubble mode, discrete bubbles departed from the heater array with a waiting time between the departure of a bubble and nucleation of the next. In multiple bubble mode, bubble nucleation occurred immediately after the previous bubble departed. The departing bubble sometimes pulled the growing bubble off the surface prematurely and the bubbles merged vertically forming small vapor columns. The data indicated that the area influenced by a single bubble departing the surface was approximately half the departure diameter. Microlayer evaporation was observed to contribute a significant, but not dominant, fraction of the wall heat transfer in the single bubble mode where a long waiting time preceded bubble nucleation. Microlayer evaporation was insignificant in the multiple bubble mode, and heat transfer occurred mainly through transient conduction and/or microconvection during liquid rewetting as the bubble departed the surface.

This study extends the previous work to bubbles nucleating on a surface operated under *constant wall heat flux* conditions. Wall temperature distributions were measured throughout the bubble nucleation and departure cycle using an array with microheaters 100 μm in size, and were synchronized with high-speed videos. The wall-to-fluid heat transfer was then obtained by numerically computing the heat lost to the substrate and subtracting this from the input heat. A description of the experimental apparatus, results, and implications for modeling boiling heat transfer are presented.

2. Experimental apparatus

2.1. Heater array

The heater array in this experiment is similar to that used by Demiray and Kim [6]. The array consisted of 96 platinum resistance heaters micro fabricated in a 10×10 configuration on a 500 μm thick silica substrate (Fig. 1). After cleaning the as-received wafers, a 30 nm thick Ti adhesion layer was deposited onto the silica followed by a 400 nm Pt layer. Standard photolithography was used to pattern the photoresist, and an ion mill was used to form the individual heaters followed by a plasma ash. Gold power leads 1 μm thick were then deposited to allow connections to be made to the heaters. Each array element was square with a nominal area of 0.01 mm^2 and consisted of 2 μm wide Pt lines spaced 2 μm apart. Each heater exhibited a nominal resistance of 6 kΩ and a temperature coefficient of resistance (TCR) of 0.0019 $°C^{-1}$. Gold lines that supply power to the heaters were routed between the heaters. Because the heater lines covered only half of the substrate, images of the bubble could be obtained by looking through it.

The heater array was 1×1 mm^2 in size. Although there were some cases at higher heat flux where the bubble grew to the edge of the array, we do not believe the limited array size affected our conclusions since we could measure the microlayer contribution during bubble growth before the bubble reached the edge of the array, as well as the transient conduction contribution during rewetting.

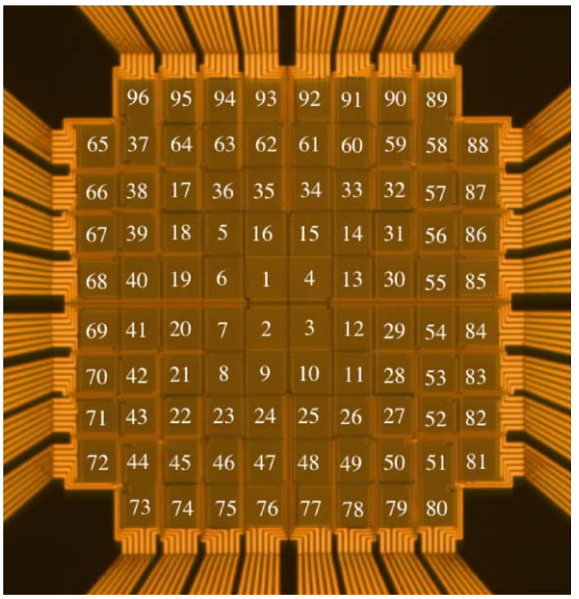

Fig. 1. Photograph of heater array indicating the heater numbering. Each heater in the array is nominally 100 microns in size.

2.2. Control circuit

Each heater was supplied with constant power by circuits consisting of a Wheatstone bridge and amplifier as shown on Fig. 2. $R1$ was similar in value to Rh, and was tailored for each circuit so all heaters dissipated similar heat fluxes for a given V_{top} (voltage supplied to the bridge). The variation in heat flux across the array was calculated to be <2% for the maximum possible temperature variation across the array. The ratio of $R2/R3$ was kept similar to $R1$/Rh at room temperature to minimize the offset voltage entering the amplifier. The analog output from each of the circuits was linearly proportional to V_{heater}. The heater power could be changed using V_{top}, and the heater current could be computed from

$$i_{heater} = \frac{V_{top} - V_{heater}}{R1} \tag{1}$$

The power dissipated by a heater is $\dot{q} = i_{heater} V_{heater}$. Although Rh changed with heater temperature, the voltage across the heater V_{heater} also changed, resulting in a power dissipation that was essentially constant over the expected operating temperature range. Twenty-four circuits were constructed on a single card, requiring four cards to control the array. The four cards were connected to a custom designed multiplexer board that set V_{top} and routed the signals between the individual circuits and the computer.

2.3. Heater calibration

Calibration of the heater array was performed using a two-step process. First, the TCR of the heaters were determined by placing the array in an oven held to within 0.1 °C of the set temperature and measuring the

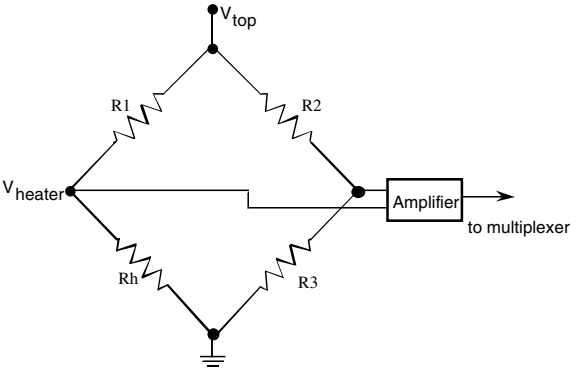

Fig. 2. Circuit schematic for one heater.

resistance of each heater from 40 °C to 100 °C. Two thermocouples attached to the underside of the heater assembly were used to ensure stability of the temperature environment.

The second step involved calibrating the measured output voltage from each heater circuit (relative to the applied power) with the resistance of the heater. The control cards and multiplexer were connected to banks of known resistors (nominally 6 kΩ, 7 kΩ, and 8 kΩ), and the output voltage of each heater circuit then measured at each resistance level. Since an amplifier's output voltage was directly correlated to the resistance of a heater, this two-step process provided measurements of heater temperature with an expected uncertainty of less than 1 °C.

2.4. Boiling Rig

The boiling rig (Fig. 3) was custom designed and built to handle FC-72, the working fluid in this experiment. The boiling chamber was a rectangular $9 \times 9 \times 14\ \text{cm}^3$ aluminum chamber with a bellows pressure control system. Three 5 cm diameter view ports allowed optical access. External surface mounted heaters (Thermo foil, Minco Products, Inc.) were attached to the chamber and covered by foam insulation to control the bulk fluid temperature. Bulk fluid temperature was measured by two T-type thermocouples placed at different heights in the chamber. Chamber pressure was measured using an absolute pressure transducer (0–345 kPa, 0.4 kPa) through an access port on one side of the chamber. Fluid access ports placed on another side of the chamber allowed mixing with an external pump if stratification was detected.

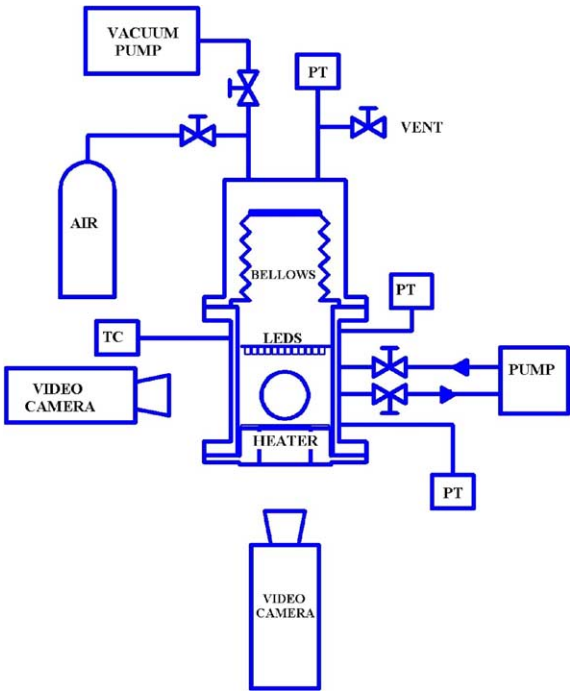

Fig. 3. Illustration of custom designed boiling rig.

2.5. Data acquisition and high speed video

A single data acquisition card (PCI-DIO96, Measurement Computing Corp.) capable of scanning 96 channels at 200 kHz was installed in a PC (Pentium III, 667 MHz) and connected directly to the custom multiplexer board. Custom software, written in C, was used to control the experiment. The combined system was capable of obtaining time resolved temperature data from each heater at a rate of 1130 Hz for a set period of time.

Temperature acquisition was synchronized with two high-speed digital video cameras. Because the heater was semi-transparent, it was possible to acquire images of the bubbles through the heater using a high-speed camera (Vision Research Phantom IV) set to acquire 256×256 resolution images. Side view images of the bubbles were obtained using a second high-speed camera (Vision Research Phantom V) at 256×256 resolution. Through the system multiplexer, the high-speed cameras were synchronized to acquire an image during the same rising edge TTL pulse from the computer. Two custom built banks of high performance LED's provided the light for each camera.

It should be noted that the heat flux dissipated at the wall is not strictly constant since 18 of the 96 heaters were non-functional (it was difficult to get all 96 heaters functioning with a line width of only 2 μm). The non-functional heaters were difficult to account for, but the conclusions we will draw from the data do not appear to be affected by their presence.

3. Numerical processing

The wall-to-liquid heat transfer can be obtained by subtracting the substrate conduction from the constant heat dissipated by the heaters. The substrate conduction was obtained using a 3-D, transient, finite difference model to determine the instantaneous temperature distribution within the substrate from which the temperature gradient at the wall, and thus the wall heat flux, could be found. The heat conduction equation was discretized using a second order central differencing scheme for the spatial coordinates and time advancement was performed using a fully implicit Euler scheme. The resulting algebraic equations were solved using the Tri-Diagonal Matrix Algorithm (TDMA) with Gauss–Seidel iteration. Thermal conductivity and specific heat were assumed to be constant in the specified temperature

range. There were no heat generation sources in the material.

3.1. Numerical model

The substrate geometry ($5.0 \times 5.0 \times 0.5$ mm^3) was discretized using a non-uniform grid along the x, y, and z directions. Along the 5.0 mm directions, 20×20 nodes were placed within the central 1×1 mm^2 area to represent the area directly under the heater array. Hence, there were 2 nodes per heater along each direction (total of 4 nodes per heater area) spaced 50 μm apart. An additional 15 nodes were placed on either side of the heater on the silica substrate spaced 133 μm apart. Along the thickness of the substrate (z-direction, 0.5 mm) 21 nodes were spaced in a geometric progression according to

$$\Delta z(i+1) = \Delta z(i)^{*}\gamma \tag{2}$$

with $\gamma = 1.05$. This ensured that the grid was very fine close to the heater array and progressively coarser away from it. The minimum grid spacing was 15 μm while the maximum was 40 μm.

The time step was 0.000885 s (corresponding to the sampling frequency of 1130 Hz). At each time step, the measured temperature at every heater was imposed as a Dirichlet boundary condition. The remaining substrate area was assumed to have a convective boundary condition with a bulk heat transfer coefficient of 200 W/m^2 K and a bulk fluid temperature of 52.7 °C. These values were found to be reasonable through FLUENT simulations. Adiabatic conditions were specified at all other faces (the side walls and the bottom face of the substrate).

3.2. Validation

Convergence was assumed when the normalized residual was less than 10^{-6}. The results were checked for grid independence and this grid was found to provide accurate results. The errors compared with numerous steady state and transient analytical heat conduction models were found to be within 0.075% for all cases.

3.3. Data processing

The algorithm solved for the temperatures at every point in the domain at each time step, from which the instantaneous heat flux distribution at the substrate surface was computed. The heater-to-fluid heat flux at every time step could then be found by subtracting the substrate conduction from the heat supplied to each heater. This data along with the digital images obtained during the experiment were then imported into MATLAB from which images colorized using temperature and heat flux data were produced.

4. Results: wall temperature

Distilled and degassed FC-72 was used as the working fluid. The voltage at the top of the bridge was initially set to a high value (V_{top} between 8.7 V and 10 V) for 3.5 s to initiate nucleation on the surface, after which it was dropped to a set value (V_{top} between 6.2 V and 8.3 V) for 14.2 s. The bulk fluid temperature was 52.3 ± 0.2 °C and the dissipative heat flux supplied to the array ranged from 14 W/cm^2 to 25 W/cm^2.

Spatially averaged temperatures of the middle 64 heaters vs. time at four voltages are shown on Fig. 4. Frame 0 corresponds to when the voltage drops to the set value, with each subsequent frame obtained at 0.000885 s intervals (1130 Hz acquisition rate). All of the heater temperatures initially decay as a result of the drop in voltage, but then approach a steady value. Visual observation of the boiling behavior indicated that only a single bubble was observed on the surface for $V_{top} \leqslant 6.8$ V. For the 6.2 V case, nucleation ceased altogether beginning from frame 1450, resulting in an increase in the wall temperature as the wall adjusted to the natural convection above the heater. Oscillations in the temperature were seen when bubbles were present on the surface. Multiple bubbles were observed to coexist on the surface for $V_{top} \geqslant 7.1$ V. For the 8.3 V case, multiple satellite bubbles surrounding a single large bubble and merging with it were observed.

Nucleation was not observed for $V_{top} < 6.2$ V ($\Delta T_{sat} < 34$ °C). The high wall superheat required for bubble nucleation is probably due to numerous factors, including the wettability of FC-72 on the heater surface, the thorough degassing of the fluid that was performed,

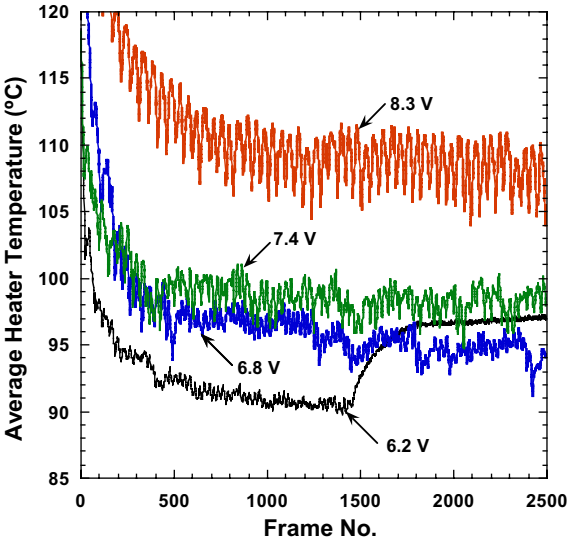

Fig. 4. Average heat transfer from middle 64 heaters.

the relatively smooth surface of the microheater array produced by micorfabrication process, and the 1 μm thick SiO_2 passivation layer. This superheat is not unreasonable, however. For example, consider the data of Cooper and Lloyd [2] who studied single bubble heat transfer using toluene and isopropyl alcohol. At their operating pressures of 6.9 kPa and 13.8 kPa, toluene boils at 37 °C and 53 °C, respectively, while isopropyl alcohol boils at 28 °C at 6.9 kPa. The only indication of wall temperature in their experiments (given on Fig. 2 of their paper) indicates an average temperature of about 70 °C. For this wall temperature, the wall superheats for toluene at the two pressures can be computed to be 33 °C and 17 °C, while the superheat for isopropyl alcohol is 42 °C. The wall superheats in the current study are approximately 34 °C, similar to Cooper and Lloyd's [2] values. An estimate of the homogeneous nucleation temperature can be obtained using the Berthelot equation of state

$$\left(P_r + \frac{3}{T_r v_r^2}\right)\left(v_r - \frac{1}{3}\right) = \frac{8}{3}T_r \tag{3}$$

along with the stability criterion $\partial P_r/\partial v_r|_{T_r} = 0$ to obtain the spinodal curve. For FC-72 (T_{cr} = 178.5 °C and P_{cr} = 18.16 atm, respectively), the limiting temperatures can be computed to be about 143 °C, so the observed superheats are well below the homogeneous nucleation temperature.

4.1. Temperature variations due to single bubbles

Single bubbles regularly departing one after another were observed for the 6.2 V, 6.5 V, and 6.8 V cases (dissipative heat fluxes of 14, 15, and 16 W/cm^2, respectively). Images (frames 825–859) of a bubble nucleation and departure event for the 6.8 V case are shown on Fig. 5 where every other frame of the high-speed video is presented. Each heater has been colored according to its temperature (non-functional heaters are not colored). The dark rings that are clearly visible in the images result from shadows cast by the growing bubble. It can be shown from simply ray tracing (see Yin et al. [7]) that the outer diameter of this ring corresponds to the diameter of the bubble while the thickness of the ring depends on the bubble shape. A thin ring indicates the bubble shape is close to being hemispherical. Thicker rings result from a more spherical bubble. The inside diameter of the ring can also be representative of the dry spot size.

Departure of a bubble is observed in frames 825–831. The outer diameter of the ring remains roughly constant while the inner diameter decreases, indicating rewetting of the dry spot by liquid as the bubble departs the surface. Nucleation and rapid growth of a new bubble are observed in frames 831–841. The images show that the bubble grows hemispherically through Frame 841, as indicated by the thin, dark ring to a maximum diameter of about 900 μm. The bubble takes about 7 ms to reach this size from nucleation—this is significantly slower than was observed for a similar bubble growing on a constant temperature surface for which it took less than 2 ms to reach its maximum size [6]. It is believed that a dry spot forms on the wall under the bubble during this time. The bubble then becomes progressively more spherical as indicated by the thickening of the ring (frames 841–856) during which liquid rewets the surface. Bubble departure occurs at frame 856 (not shown) after which a new bubble immediately nucleates and grows.

The temperature of the heaters directly under the growing bubble *increase* during initial hemispherical bubble growth (frames 831–841), indicating that the energy extracted from the wall is smaller than the electrical energy supplied to the heater. The heaters under the bubble continue to increase in temperature once a dry spot forms since power is continually supplied to them while little energy is removed by the low thermal conductivity vapor (frames 841–856). These same heaters are observed to decrease in temperature as they are rewet by liquid as the bubble departs the surface (frames 851–856). Temperature variations as large as 8 °C occur for a given heater in the array due to bubble growth and departure.

The spatially averaged temperature of the middle 64 heaters vs. time over a small time interval are shown on Fig. 6–the frames at which the individual bubbles depart the surface, and those at which the bubble diameter reaches a maximum are indicated. The wall temperature increases during nucleation and growth of a bubble on the surface, and decreases as the surface is rewet by liquid during bubble departure. Clearly, rewetting of the surface is associated with higher wall heat transfer. The bubble departure frequency is ~44 Hz for the three power levels shown.

4.2. Temperature variations due to bubble coalescence

Bubble coalescence was observed for $V_{top} \geqslant 7.1$ V (dissipative heat flux of 18 W/cm^2). Images of the bubble behavior along with the temperature distribution are shown on Fig. 7 for 7.1 V. A bubble departure event occurs on frame 672. Nucleation and growth of a new bubble occurs beginning on frame 673 (not shown). The bubble reaches its maximum size on frame 681 (not shown), then begins to depart. During this departure process, a new bubble nucleates under this departing bubble (frame 684, lower right corner), grows, and coalesces with the departing bubble (frame 690). The coalesced bubble then departs. Nucleation and growth of three new bubbles then occurs beginning frame 692. Two of these bubbles coalesce in frame 696 (middle and upper left) while the third bubble continues to grow in the lower right. Coalescence of the third bubble with

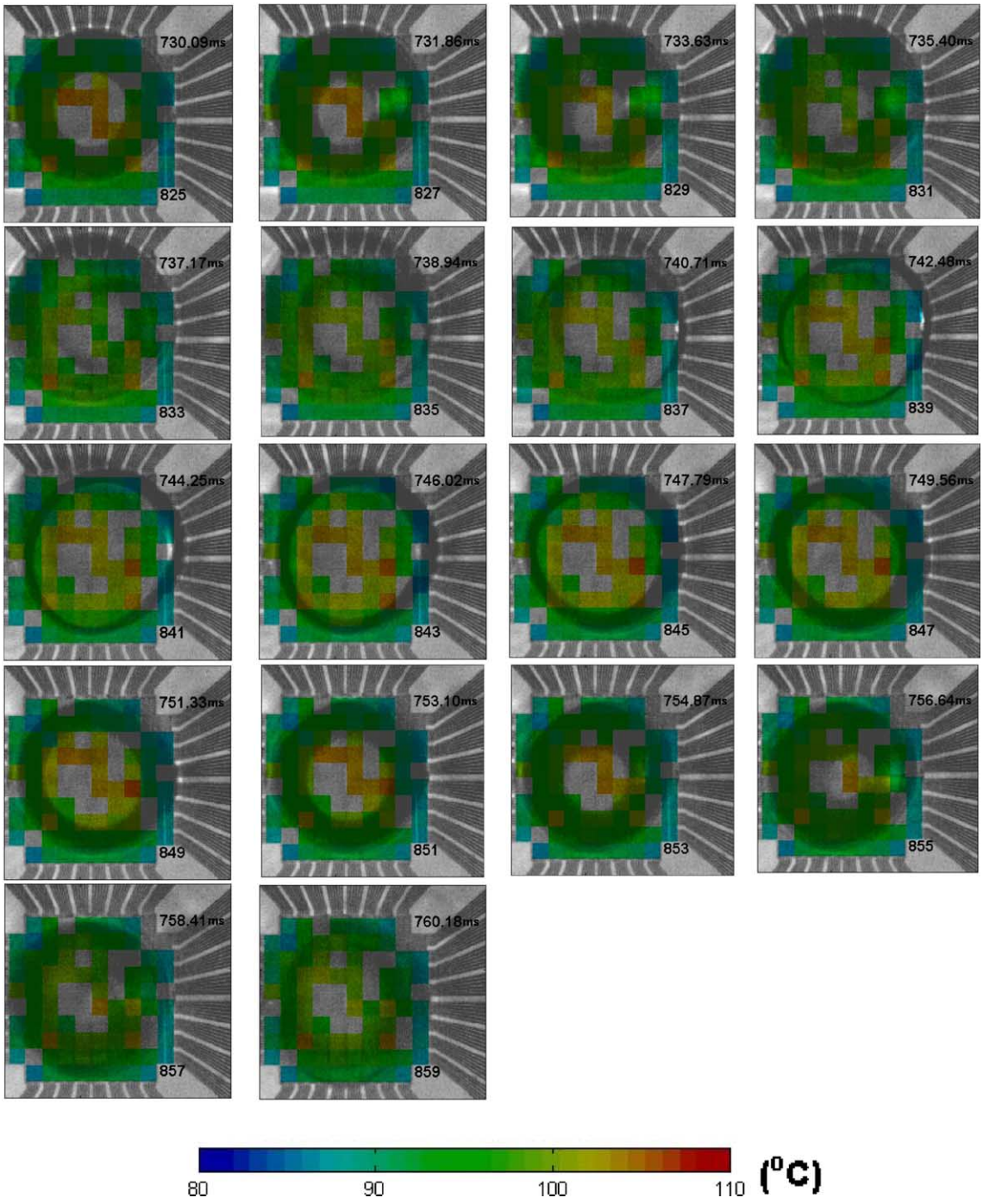

Fig. 5. Surface temperature distribution through one bubble nucleation and departure cycle, 6.8 V. The time and frame numbers are given in the upper right and bottom right respectively of each frame.

the previously coalesced bubble occurs beginning frame 712. The maximum bubble size occurs in frame 716, after which the bubble begins to depart the surface. Bubble departure occurs on frame 726. The average heater temperature during this series of events is shown on Fig. 8. Bubble departure, maximum bubble dry area, and coalescence events are noted. Coalescence events are seen to cause small drops in the heater temperature, but

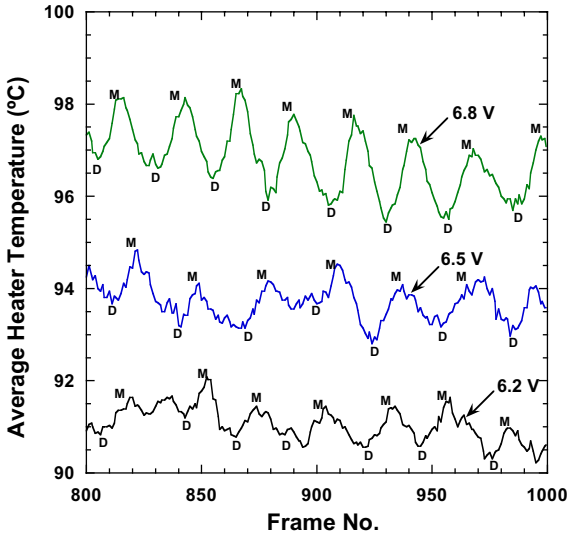

Fig. 6. Temperature oscillations on the surface due to single bubble nucleation and departure at low voltages (D = bubble departure, M = maximum dry area).

bubble departure is observed to cause the largest drop. Coalescence may become more significant at higher heat fluxes when bubble merger occurs more frequently. Bubble coalescence can also lead to earlier departure of bubbles due to the increased size of the coalesced bubbles [8], indirectly leading to higher wall heat transfer.

The bubble behavior for 8.3 V (dissipative heat flux of 25 W/cm^2) was very chaotic. Numerous bubbles could exist on the surface simultaneously, and these bubbles coalesced as they grew. The coalesced bubble moved randomly on the heater as it coalesced with other satellite bubbles, eventually forming a single large bubble on the surface under which dry out occurred. The departure frequency of the coalesced bubble was much lower than that of individual bubbles. Departure of the coalesced bubble occurred occasionally, but there was no precisely defined bubble pinch-off event. As the coalesced bubble rewet the surface during departure, the wall temperature was hot enough to cause nucleation within the liquid front as it rewet the surface. Bubbles growing under the departing bubble and merging with it were observed. Fluctuations in average wall temperature through a few departure cycles are shown on Fig. 9. Again, large drops in wall temperature are associated with departure of the coalesced bubble, and high temperatures correlate with maximum dry area.

5. Results: wall heat flux

Heat flux behavior is discussed next. All heat flux values have been corrected for substrate conduction calculated numerically as discussed earlier. The uncertainty in the wall heat transfer is larger than in earlier constant wall temperature work since the heat flux is computed by taking the derivative of the temperature variations, and is estimated to be 15%.

5.1. Heat flux variations

The time variation of the spatially averaged heat flux over the middle 64 heaters (6.8 V) is shown on Fig. 10 for the bubble nucleating on frame 831. The heat flux is initially large due to departure of the previous bubble (frame 831). The heat flux then decreases as a new bubble nucleates and grows, and reaches a minimum around the time the dry area under the bubble reaches its maximum size (frame 841). The heat flux increases again as liquid rewets the surface as the bubble departs (frame 856). The variations in the space averaged heat flux are about 5 W/cm^2.

5.2. Heat flux variation due to single bubble departure

Space resolved heat flux during a bubble nucleation and departure event for the 6.8 V case are shown on Fig. 11 where every other frame of the high-speed video is presented. Each of the heaters has been colored according to the surface heat flux. Non-functional heaters are not colored. During bubble growth (frames 831–841), the wall heat transfer under a nucleating bubble decreases as the microlayer evaporates. The heat transfer under the dry spot that subsequently forms (frames 841–851) is very low as expected due to the low thermal conductivity of the vapor. Once the bubble departure process begins and liquid rewets the surface, the heat transfer from the heaters under the advancing contact line increases, and the peak heat flux occurs just as the bubble departs (frame 856). The wall heat flux drops again after the next bubble nucleates. These results are consistent with those obtained in previous works [5,6] when the heaters were operated in constant wall temperature mode.

5.3. Bubble heat transfer mechanisms

Microlayer evaporation occurs when a thin liquid layer trapped under a growing bubble evaporates. The heat transfer at the receding contact line can be thought to be part of this mechanism. An upper bound on the contribution of microlayer evaporation to bubble growth can be obtained by integrating the heat transfer from all heaters under the growing bubble at each time step. The heaters outside of the projected bubble area are assumed to be cooled by transient conduction/microconvection. Once the bubble reaches its maximum extent and begins to depart, microlayer evaporation is assumed to cease. The contact line heat transfer is also assumed

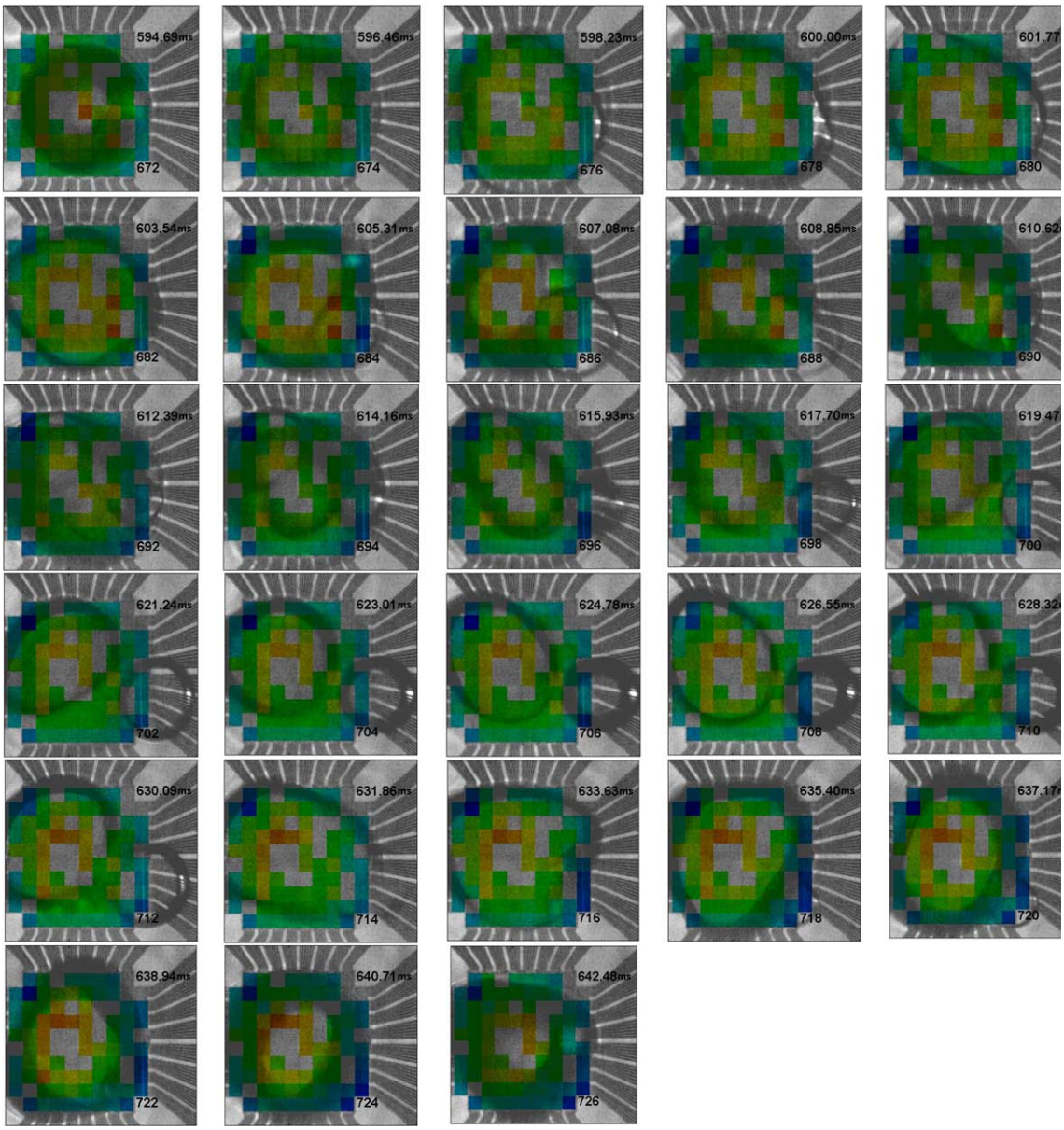

Fig. 7. Surface temperature distribution through a bubble coalescence event, 7.1 V. The time and frame numbers are given in the upper right and bottom right respectively of each frame. The temperature scale is the same as shown on Fig. 5.

to cease since the contact angle increases [9], and heat is transferred only by transient conduction/microconvection. A plot of the heat transfer contribution due to the microlayer and transient conduction/microconvection computed this way during a bubble departure cycle is shown on Fig. 12. The microlayer heat transfer peaks at Frame 841, then drops to zero once the bubble begins to depart. Transient conduction/microconvection is large at bubble nucleation due to departure of the previous bubble, then drops to near zero as the bubble grows and covers the almost all of the heated area. Once the bubble begins to depart, transient conduction/microconvection increases until bubble departure. The total energy transferred by each mode can be obtained by integrating the heat transfer from bubble nucleation to a given time (Fig. 13). About half of the energy transferred from the wall at the end of bubble growth (frame 841) is due to microlayer evaporation. Over the bubble departure cycle, microlayer evaporation contributes at most 23% of the total energy transferred from the wall.

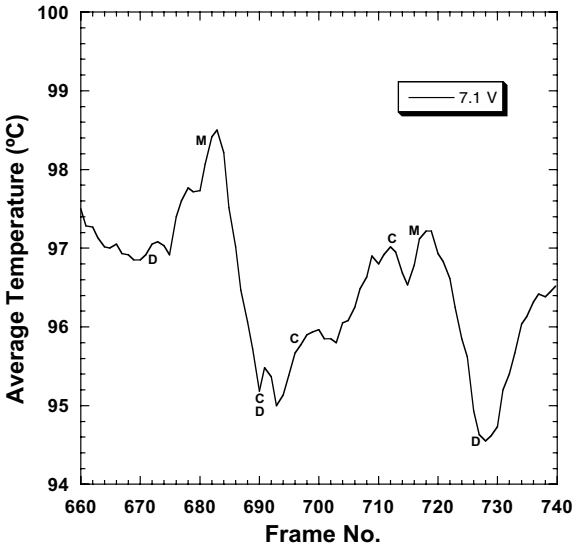

Fig. 8. Average heater temperature during bubble coalescence (D = bubble departure, M = maximum dry area, C = coalescence event).

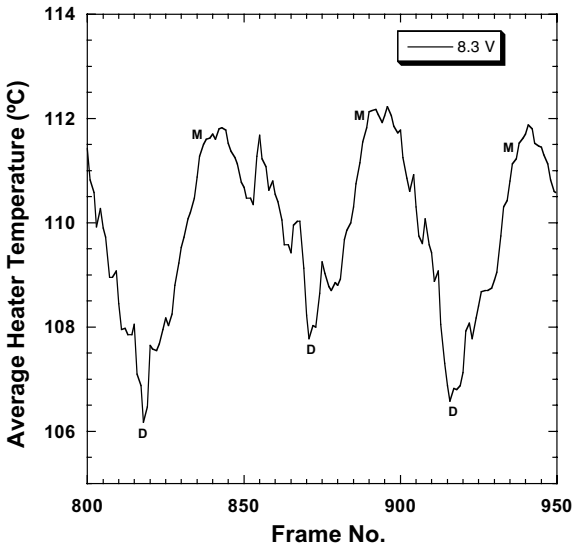

Fig. 9. Average heater temperature during bubble coalescence (D = bubble departure, M = maximum dry area), 8.3 V.

The heat transfer data can be used to compute an equivalent bubble diameter (d_{eq}) by assuming all the heat transferred from the wall appears as latent heat:

$$\rho_v \frac{\pi d_{eq}^3(t)}{6} h_{fg} = \int_0^t \dot{q}''_h(t) A_h \, dt \Rightarrow$$
$$d_{eq}(t) = \sqrt[3]{\frac{6}{\pi \rho_v h_{fg}} \int_0^t \dot{q}''_h(t) A_h \, dt} \quad (4)$$

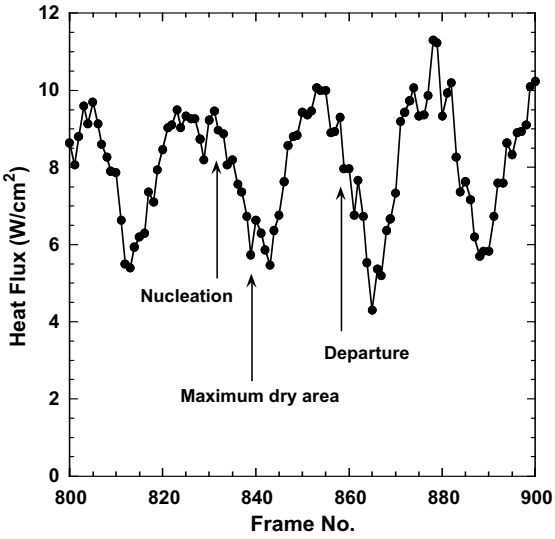

Fig. 10. Spatially averaged heat flux over the middle 64 heaters, 6.8 V.

where $\dot{q}''_h(t)A_h$ is the heat transfer from heater [W]. d_{eq} is compared with the actual measured bubble diameter on Fig. 14 for two bubble departure cycles. For the bubble nucleating on frame 831, the size of the bubble that forms on the surface is much larger than can be accounted for by microlayer evaporation, especially during the early growth period. The bubble must have gained the majority of its energy from the superheated liquid layer. For the bubble nucleating on frame 715, the measured diameter is much larger than the equivalent diameter during bubble growth, clearly indicating that the bubble size cannot be accounted for by the wall heat transfer.

In summary, the results described above are not consistent with a microlayer evaporation dominated boiling heat transfer mechanism, which predicts large heat transfer rates during bubble growth just after nucleation. The heat transfer after nucleation actually decreased, indicating that bubble growth and wall heat transfer are not correlated. The results are also not consistent with contact line heat transfer dominated boiling. It would be expected from contact line theory that the heat transfer as the bubble grows (receding contact line and smaller contact angles) would be higher than when the bubble departs (advancing contact line and larger contact angles) if liquid flow to the meniscus were not limited, but this was also not observed. Transient conduction into the rewetting liquid appears to be the dominant heat transfer mode. Other studies which attempted to quantify the contribution of various heat transfer mechanisms to boiling [10–13] have also indicated that microlayer evaporation

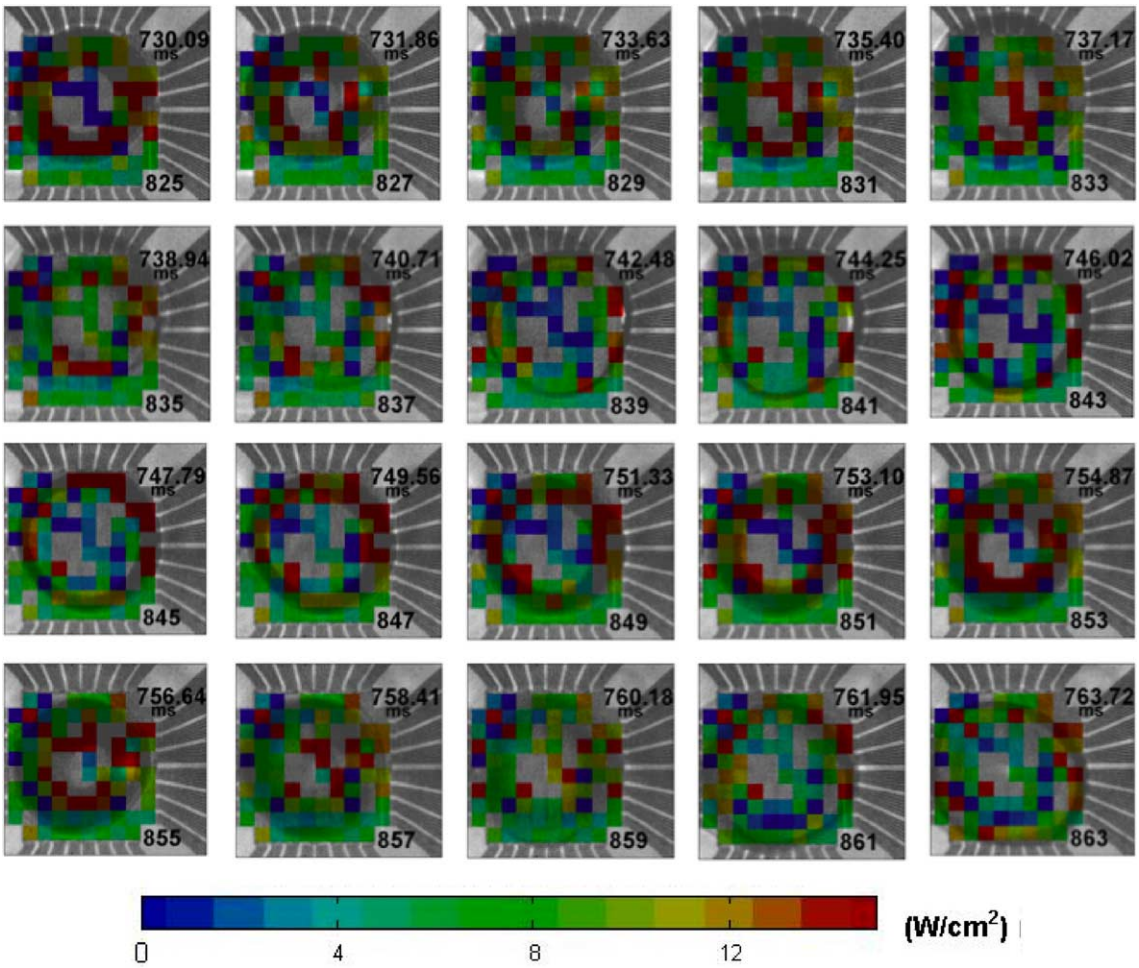

Fig. 11. Heat transfer distribution on surface through a bubble nucleation and departure cycle, 6.8 V. The time and frame numbers are given in the upper right and bottom right respectively of each frame.

contributes not more than 50% of the overall heat transfer.

It is unclear why the current results are different from those of Cooper and Lloyd [2] and Moore and Mesler [14], who concluded that microlayer evaporation was the dominant heat transfer mechanism. The data of Cooper and Lloyd [2] indicates that the wall temperature drops as the bubble grows and the microlayer evaporates, then increases after a dry spot forms. Another small drop in temperature occurs as the wall is rewet as the bubble departs, then increases as the thermal boundary layer is reestablished. We see similar trends, but the microlayer contribution to the total heat transfer is much smaller. One possible explanation of the discrepancy between the two studies is the difference in the Jakob number, *Ja*. *Ja* for FC-72 at $\Delta T_{sat} = 34\ ^{\circ}C$ is about 0.42. For the data of Cooper and Lloyd [2], toluene at 6.9 kPa and $\Delta T_{sat} = 33\ ^{\circ}C$ corresponds to $Ja = 0.13$, while isopropyl alcohol at 6.9 kPa with $\Delta T_{sat} = 42\ ^{\circ}C$ corresponds to $Ja = 0.15$ (the average wall temperature was assumed to be 70 °C as indicated in Fig. 2 of their paper). The larger *Ja* values for the current results suggests that sensible heating of the liquid is more important than microlayer evaporation than in the data of Cooper and Lloyd [2], consistent with the observations.

5.4. Transient conduction model

A simple 1-D transient conduction model for advancing contact line heat transfer can be used to predict the wall heat transfer during bubble departure. Consider the case of a 1-D liquid front rewetting a heater at temperature T_w (Fig. 15). It is assumed that the heat transfer at the advancing three-phase contact line is negligible. The liquid is at temperature T_l far from the wall. The heat

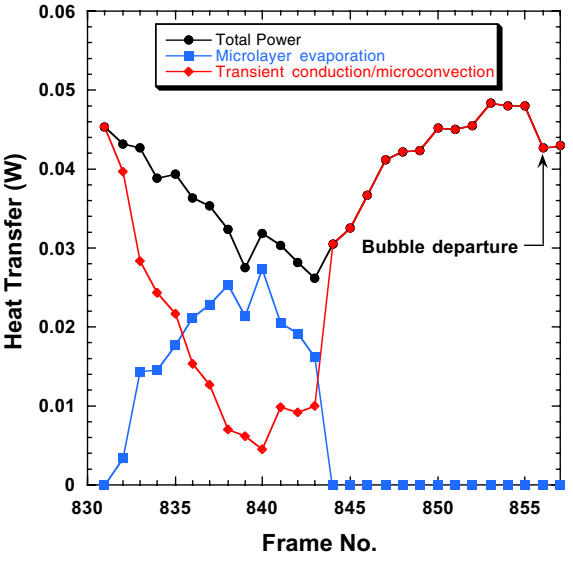

Fig. 12. Wall-to-fluid heat transfer contribution during a bubble departure cycle, 6.8 V.

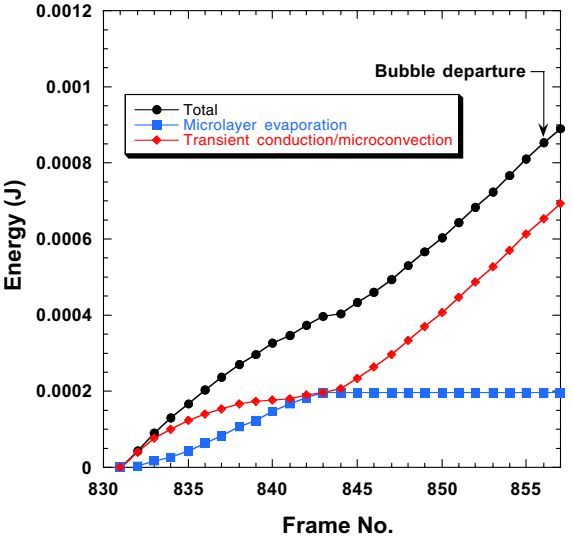

Fig. 13. Energy transferred through a bubble departure cycle, 6.8 V.

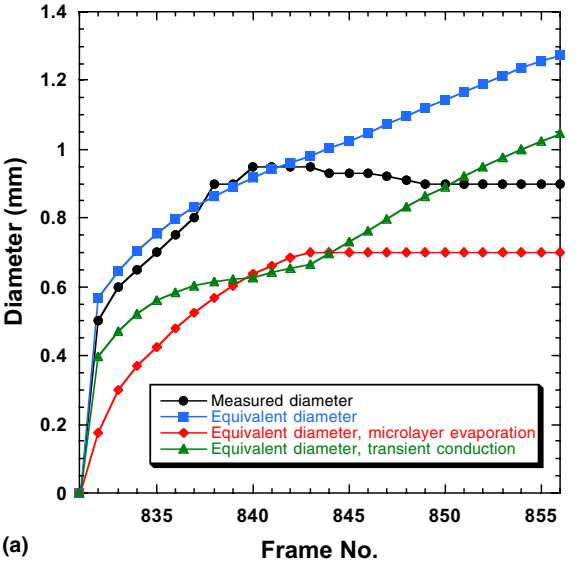

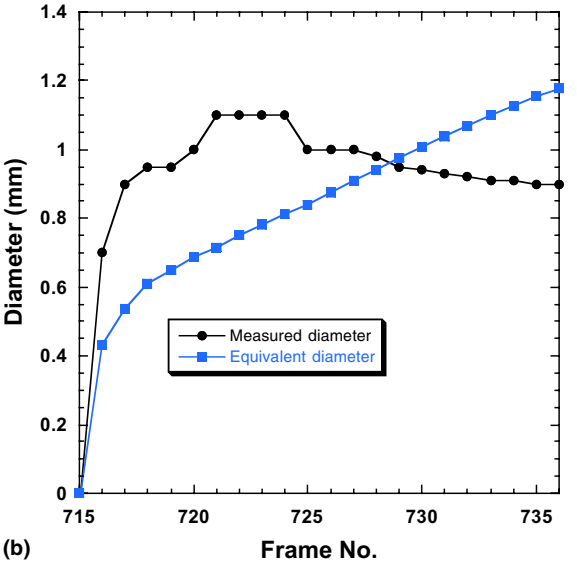

Fig. 14. Measured vs. equivalent diameters for two bubbles. Bubble nucleating on frame 831 (a) and 715 (b).

flux at any position covered by liquid is obtained from the solution for transient conduction into a semi-infinite solid:

$$\dot{q}'' = \frac{k(T_w - T_l)}{\sqrt{\pi\alpha_l t}} \tag{5}$$

where t is the length of time the liquid has been covering a particular location on the heater. For a circular advancing contact line, assume the dry patch under a bubble has initial radius r_0 and this dry patch decreases in size allowing liquid to rewet the surface as occurs during the bubble departure process. At time t, a position $r' < r_0$ has been wetted for time $t - t'$. The heat flux at r' is

$$\dot{q}'' = \frac{k(T_w - T_l)}{\sqrt{\pi\alpha_l}} \frac{1}{\sqrt{t - t'}} \tag{6}$$

and the wall heat transfer at time t is

$$\dot{q} = \int_0^r \frac{k(T_w - T_l)}{\sqrt{\pi\alpha_l}} \frac{2\pi r' \, dr'}{\sqrt{f(r) - f(r')}} \tag{7}$$

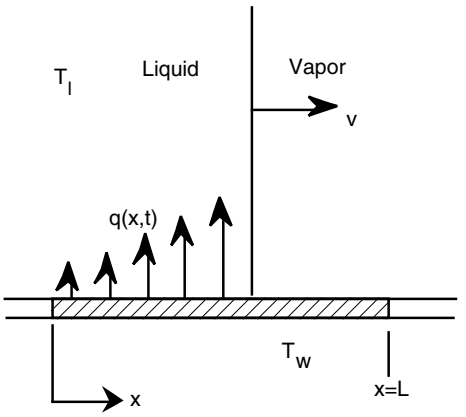

Fig. 15. Transient conduction model.

For the special case where the dry patch diameter shrinks linearly with time ($r = r_0 - vt$), the wall heat transfer can be shown to be

$$\dot{q} = \frac{4\pi k(T_w - T_l)\sqrt{v}}{\sqrt{\pi\alpha_l}}\left[\frac{1}{3}(r_0 - r)^{3/2} + r(r_0 - r)^{1/2}\right] = \frac{4\pi k(T_w - T_l)\sqrt{v}}{\sqrt{\pi\alpha_l}}\left[\frac{1}{3}(vt)^{3/2} + (r_0 - vt)(vt)^{1/2}\right] \quad (8)$$

A plot of the dry spot diameter (Fig. 16) indicates that it can be fit reasonably well using a straight line. Using this fit, the wall heat transfer can be used to obtain the heat transfer variation. The heat transfer predicted from the conduction analysis (Fig. 16) is much larger than the measured values if the temperature of the liquid rewetting the surface is close to the bulk temperature (e.g., T_{liquid} = 65 °C case). It may not seem possible that the measured heat transfer can be lower than that for transient conduction since any convection or contact line heat transfer should *increase* the wall heat transfer above that for transient conduction. However, it is likely that the liquid rewetting the wall is not from the bulk but from the superheated layer surrounding the bubble, resulting in a smaller ($T_w - T_l$) and heat transfer than predicted by the analysis. This has also been observed in numerical simulations of bubble behavior [8]. A liquid rewetting temperature of 87.5 °C results in good agreement between the predicted and measured heat transfer.

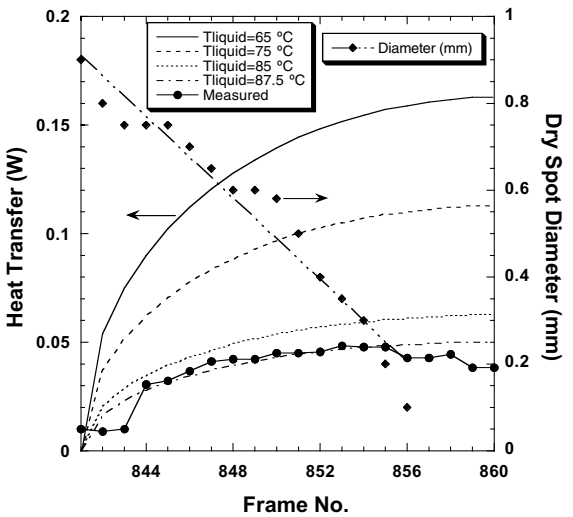

Fig. 16. Predicted vs. measured heat transfer (left ordinate). Dry spot diameter with linear fit (right ordinate).

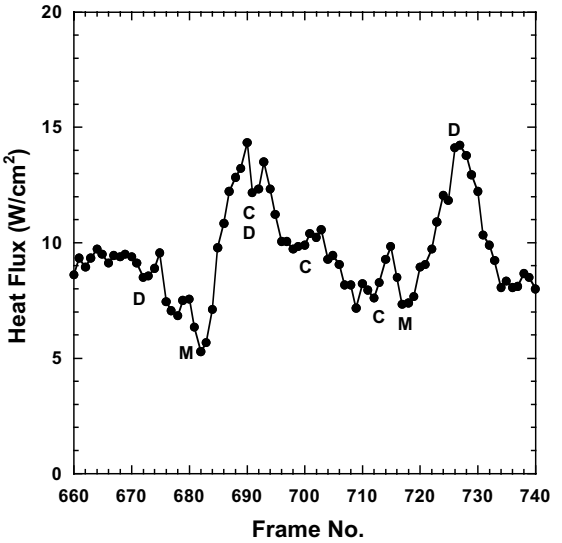

Fig. 17. Heat transfer averaged over the middle 64 heaters during bubble coalescence events (D = bubble departure, M = maximum dry area, C = coalescence event).

5.5. Heat flux due to bubble coalescence

The heat transfer during numerous bubble coalescence events are shown on Fig. 17. It is observed that bubble coalescence results in small spikes in heat transfer (~1–2 W/cm^2), but the heat transfer due to coalescence events are quite small compared to the much larger variations due to bubble growth and departure. As mentioned earlier, however, bubble coalescence can lead to earlier departure of bubbles due to the increased size of the coalesced bubbles, indirectly leading to higher wall heat transfer.

6. Conclusions

Time and space resolved temperature measurements correlated with high-speed images of bubble nucleation, growth, and departure in FC-72, were obtained using a microheater array consisting of 96 100 × 100 μm^2 heaters

operated at constant heat flux. Wall-to-fluid heat fluxes were numerically obtained. For the conditions studied, the data indicate that microlayer evaporation and contact line heat transfer are not major heat transfer mechanisms for bubble growth. The dominant heat transfer mechanism appears to be transient conduction into the liquid as the liquid rewets the wall during the bubble departure process.

Acknowledgements

This work was supported by the Office of Biological and Physical Research at NASA Headquarters, Grant No. NNC04AA26A. The grant monitor is Mr. John McQuillen.

References

[1] B.B. Mikic, W.M. Rosenhow, Bubble growth rates in non-uniform temperature field, Prog. Heat Mass Transfer II (1969) 283–292.
[2] M.G. Cooper, A.J.P. Lloyd, The microlayer in nucleate boiling, Int. J. Heat Mass Transfer 12 (1969) 895–913.
[3] P. Stephan, J. Hammer, New model for nucleate boiling heat transfer, Heat Mass Transfer/Waerme-und Stoffuebertragung 30 (2) (1995) 119–125.
[4] P.C. Wayner, Y.K. Kao, L.V. LaCroix, The interline heat transfer coefficient of an evaporating wetting film, Int. J. Heat Mass Transfer 19 (1976) 487.
[5] N. Yaddanapudi, J. Kim, Single bubble heat transfer in saturated pool boiling of FC-72, Multiphase Sci. Technol. 12 (3–4) (2001) 47–63.
[6] F. Demiray, J. Kim, Microscale heat transfer measurements during pool boiling of FC-72: effect of Subcooling, Int. J. Heat Mass Transfer 47 (2004) 3257–3268.
[7] Z. Yin, A. Prosperetti, J. Kim, Bubble growth on an impulsively powered microheater, Int. J. Heat Mass Transfer 47 (5) (2004) 1053–1067.
[8] G. Son, N. Ramanujapu, V.K. Dhir, Numerical simulation of bubble merger process on a single nucleation site during pool nucleate boiling, J. Heat Transfer 124 (2002) 51–62.
[9] S.G. Kandlikar, M.E. Steinke, Contact angles and interface behavior during rapid evaporation of liquid on a heated surface, Int. J. Heat Mass Transfer 45 (2002) 3771–3780.
[10] R.L. Judd, K.S. Hwang, A comprehensive model for nucleate pool boiling heat transfer including microlayer evaporation, J. Heat Transfer 98 (1976) 623–629.
[11] L.D. Koffman, M.S. Plesset, Experimental observations of the microlayer in vapor bubble growth on a heated solid, J. Heat Transfer 105 (1983) 625–632.
[12] R.J. Benjamin, A.R. Balakrishnan, Nucleate pool boiling heat transfer of pure liquids at low to moderate heat fluxes, Int. J. Heat Mass Transfer 39 (1995) 2495–2504.
[13] G. Son, V.K. Dhir, N. Ramanujapu, Dynamics and heat transfer associated with a single bubble during nucleate boiling on a horizontal surface, J. Heat Transfer 121 (1999) 623–631.
[14] F.D. Moore, R.B. Mesler, The measurement of rapid surface temperature fluctuations during nucleate boiling of water, AICHE J. 7 (4) (1961) 620–624.